

Supplementary Information

Ti_{0.87}O₂ nanosheets on Ni integrated n-Si: Planar architecture with enhanced photoresponse for self-driven photodetector

Nasir Ali^a, Zhiwen Xing^a, Cheng Jia^{b,*}, Di Wu^c, Longhui Zeng^d and Huiyu Yuan^{a,*}

^a Henan Key Laboratory of High Temperature Functional Ceramics, School of Material Science and Engineering, Zhengzhou University, No.100 Science Avenue, Zhengzhou 450001, China.

^b Institute of Quantum Materials and Physics, Henan Academy of Sciences, Zhengzhou, China.

^c Key Laboratory of Materials Physics, Ministry of Education, School of Physics, Zhengzhou University, Zhengzhou, 450001, China.

^d International Joint Laboratory for Integrated Circuits Design and Application, Ministry of Education, School of Physics, Zhengzhou University, Zhengzhou, 450001, China.

E-mails: jiach25@hnas.ac.cn; hyyuan@zzu.edu.cn;

Synthesis:

Synthesis scheme is shown in Fig.S1 showing the brief steps to obtain nanosheets. The first step involves the synthesis of the KLTO using furnace. In the second step protonation of the KLTO is done in which alkali ions present between the layers are replaced by H⁺ ions and water molecules. This digestion of the acid increases the interlayer spacing as well resulting HTO material. Third step involves the exfoliation of nanosheets from HTO using TBAOH treatment. The acid base reaction between interlayer H⁺ ions and OH⁻ ions from TBAOH occurs in this step. The consumption of interlayer H⁺ ions results in the vanishing of the interlayer forces and large size TBA⁺ ions penetrate into the interlayer spacing as the replacement of H⁺ ions. This results into the exfoliation of the nanosheets.

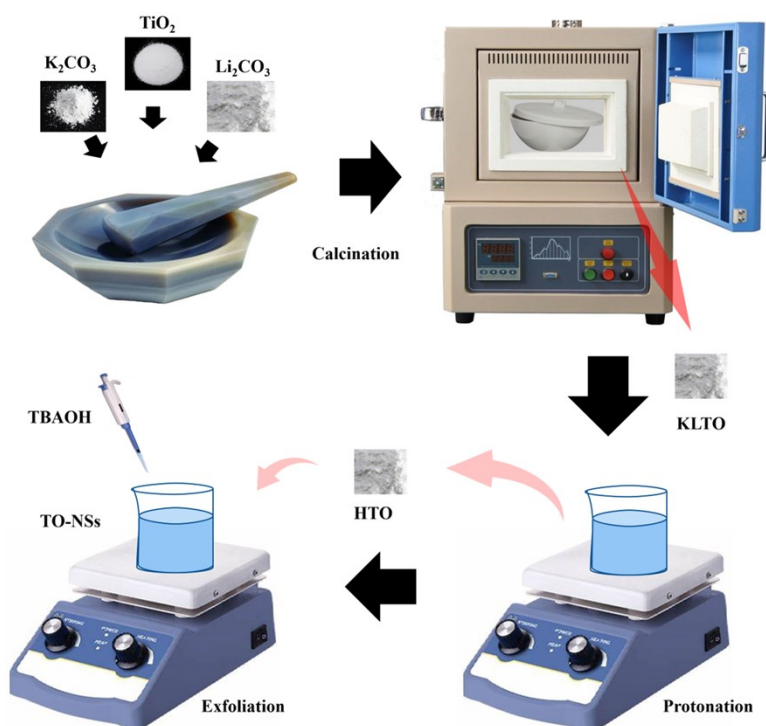


Fig. S1. Synthesis scheme. Three step synthesis process of nanosheets (a) calcination of the materials. (b) Protonation of KLTO into HTO. (c) Exfoliation of nanosheets by HTO treatment with TBAOH.

Characterization of Materials:

The morphology of the as prepared compounds was further confirmed with the scanning electron microscopy (SEM) showing synthesis of layered structure with several tens of micrometer sheet size. It is interesting to note that the protonated layered material shows large particle size due to digestion of acid between the interlayer spacing that is also confirmed by the increasing d-spacing measured through XRD of the materials. The XRD of KLTO and HTO is given Fig. S2a which is consistent the PDF cards 47-0124 and 89-5420 respectively. Fig. S2b and S2d give comparison of particle size of KLTO and HTO while Fig. S2c and S2e further confirms their layer structures respectively. Atomic force microscopy (AFM) was done after nanosheets deposition on n-Si substrate to further investigate the NSs deposition, thickness and coverage given in Fig. S2f. Densely packed assembly of several micrometers large TO NSs having greater than 96 % coverage and ~ 1.1 nm thickness depicts their suitability for optoelectronic and other applications. The actual thickness of TO NSs is ~ 0.75 nm but the presence of TBA⁺ ions on NSs during exfoliation is responsible for their thickness larger than 1 nm after deposition and the thickness of the present NSs is well matched with the reported values.

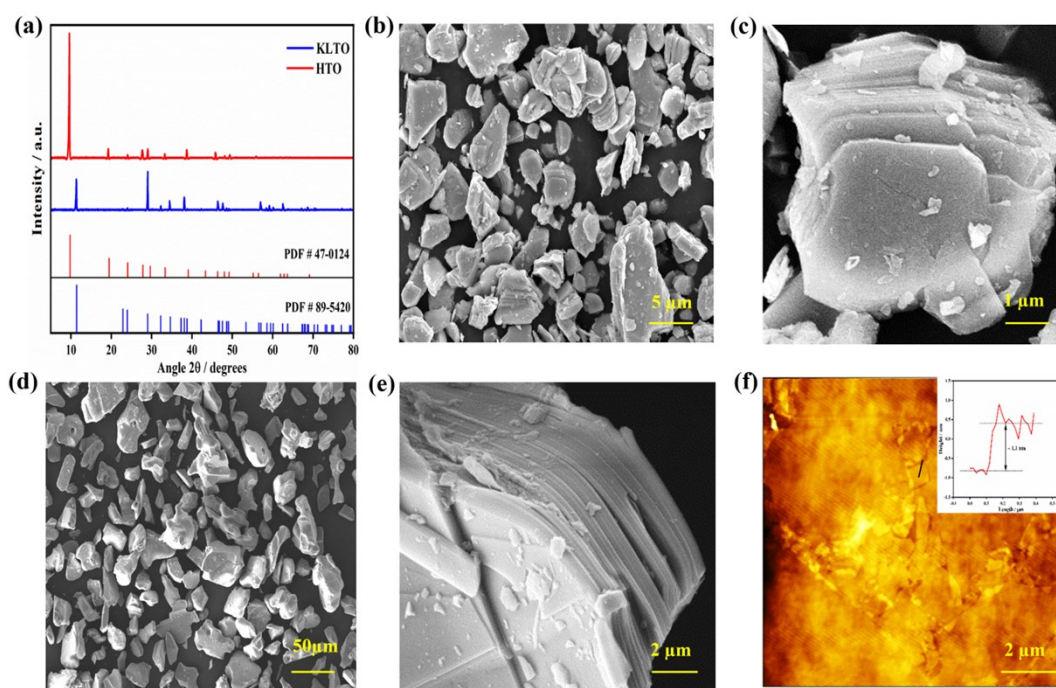


Fig. S2 Characterization of materials. (a) X-ray diffraction results of KLTO and HTO. (b) and (c) SEM of KLTO (d) and (e) SEM of HTO (f) AFM of NSs on n-Si with Thickness of TO-NSs in the inset (~ 1.1 nm).

UV-Visible Spectroscopy:

The UV-Visible spectroscopic results of KLTO and HTO with their Tauc plots has been given in the Fig. S3. Fig. S3a shows absorbance of KLTO and Fig. S3b that of HTO indicating intense absorption in UV region of spectrum due to their large band gaps. The Tauc plots of KLTO and HTO has been shown in Fig. S3d and S3e respectively. The bandgap of KLTO and HTO were found to be ~ 3.2 eV and ~ 3 eV which are consistent with the reported data. TO-NSs show intense UV-Visible absorption in UV at ~ 280 nm with bandgap of ~ 3.8 eV consistent with the literature. Conduction and valance bands of TO-NSs were measured through Mott-Schottky flat-band determination method and conduction band estimation. Respective UV-Visible curve and Tauc plot of TO-NSs have been given in Fig. S3c and S3f respectively while flat-band measurement and energy band diagram of TO-NSs are given in as shown in Fig. S3g and S3h.

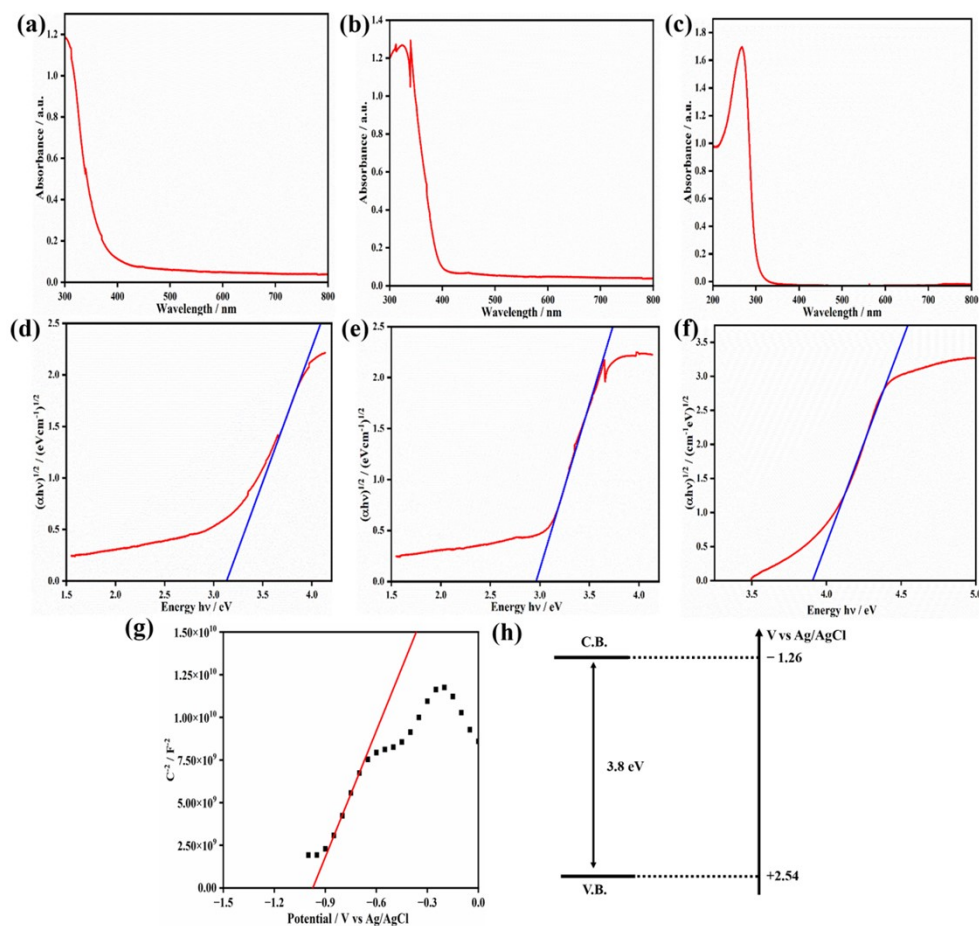


Fig. S3. UV-Visible absorbance of KLTO, HTO and TO-NSs. (a) UV-Visible absorbance of KLTO. (b) UV-Visible absorbance of HTO. (c) UV-Visible absorption curve of TO-NSs. (d) Tauc's plot of KLTO. (e) Tauc's plot of HTO. (f) Tauc's plot of TO-NSs. (g) Flat band potential measurement of TO-NSs. (h) Conduction and valance band measurement of TO-NSs.

Langmuir-Blodgett Deposition:

The exfoliated nanosheets were then used in LB method to deposit on the substrate which provides precise control of the size, thickness, and structural uniformity of the nanosheets.¹⁻⁴ The process is shown graphically in Fig. S4 where step 1 illustrates one side deposition and step 2 the other side deposition. LB technique enables the preparation of high-quality nanosheets with precise control over molecular arrangement and thickness, ensuring consistent and reliable device performance which is evident from AFM data given in Fig. S2f on Si, Fig. 4h, 4i on Ni/n-Si, SEM data of monolayer and bilayer assemblies given in Fig 4f and 4g on Ni/n-Si respectively.

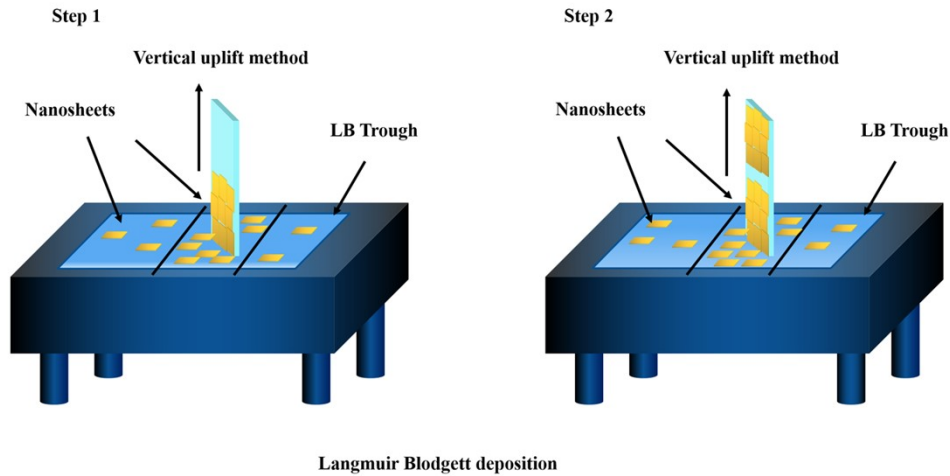


Fig. S4. LB deposition of the Nanosheets for device fabrication. Vertical uplift by Langmuir Blodgett deposition method. (a) deposition from one end. (b) Deposition from the other end.

Ni thickness effect on Photocurrent:

Ni thickness was controlled by sputtering parameters and effect of thickness on detector performance was studied through I-t curves obtained. The testing of n-Si without Ni shows no PTE response. As the thickness of Ni increases on n-Si, the photocurrent increases. The I-t curves given in Fig. S5 shows a comparison of photocurrent with 22 nm, 40 nm and 58 nm thickness of the Ni. The photocurrent with 40 nm Ni thickness is much higher than 22 nm Ni thickness. This is due to the enhanced light absorption with the increasing thickness of Ni which results in the increasing PTE effect. The photodetector performance with 40 nm Ni gives high photoresponsivity and EQE. Meanwhile, 22 nm thickness shows current suppression both in light and the dark. Dudi et al. also reports the increasing hot carriers with increase in thickness of Ni.⁵ Wu et al. reported that with the increase in thickness of metal, energy lost in the form of heat is absorbed by metal generating hot electrons.⁶ Thermoelectric field sets up potential difference due to PTE effect collects more electron which shows higher current in the external field. However, upon further increase in thickness at ~58 nm, decrease in photocurrent has been observed which may attribute due to the loss of transparency leading to low response of n-Si. Photoresponse with thicknesses of 22 nm, 40 nm, and 58 nm with AFM shown in Fig. S5a, S5b, and S5c are given in Fig. S5d, S5e, and S5f respectively.

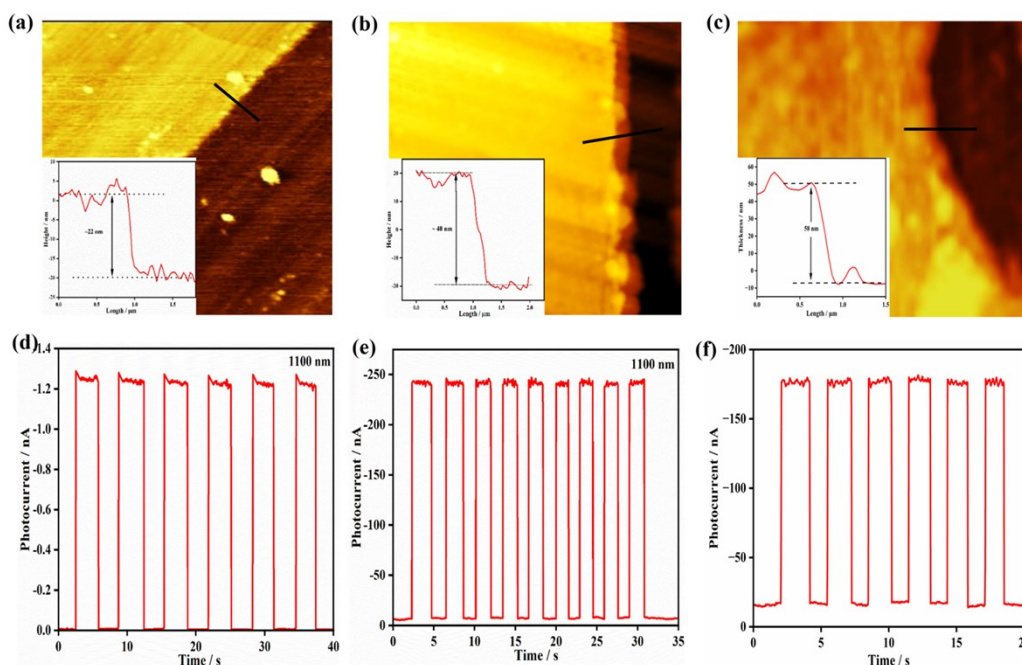


Fig. S5 Ni thickness effect on photocurrent of the device. AFM and I-t results of Ni thickness (a) AFM of Ni with 22 nm thickness. (b) AFM of 40 nm thickness of Ni. (c) AFM of 58 nm thickness of Ni. (d) I-t of the device with 22 nm thickness. (e) I-t of the device with 40 nm thickness. (f) I-t of the device with Ni thickness of 58 nm.

Effect of contact engineering:

Effect of hybrid TO-NSSs/Ag electrode on dark current is evident from Fig. S6a and S6b which clearly shows the increased contact resistance of the device. The I-t curve at 400 nm illumination on monolayers TO given in Fig. S6a shows a large dark current of ~ 20 nA of Ni/n-Si device. However, TO/Ni/n-Si device having hybrid contact have low dark current compared to the Ni/n-Si device which is evident from Fig. S6b. This suggests the effectiveness of hybrid electrodes for the application of dark current suppression in device with ohmic contacts at 0 V.

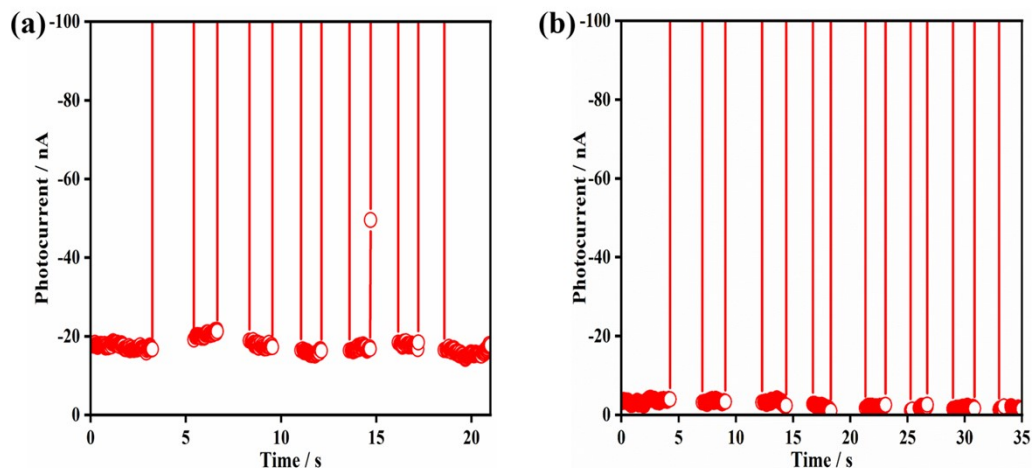


Fig. S6. Effect of hybrid electrodes on dark current of the device. (a) I-t curve showing dark current of Ni/n-Si device. (b) I-t curve showing dark current of TO/Ni/n-Si device.

Effect on Detectivity:

Detectivity of the photodetectors greatly affected by dark current. The suppression of the dark current significantly enhance the detectivity of the TO/Ni/n-Si device. It is evident from Fig. S7 that the detectivity of Ni/n-Si device is increased from $\sim 10^{12}$ Jones to $\sim 10^{13}$ Jones with highest detectivity at 400 nm illumination with the value of 2.02×10^{13} Jones.

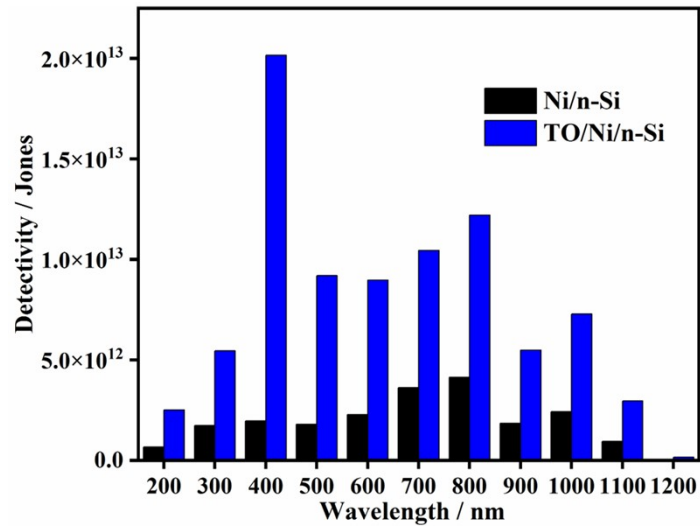


Fig. S7. Detectivity comparison of Ni/n-Si and TO/Ni/n-Si device.

Comparison of Response time:

Response time of detector depends structure, mechanism, and applied biasing of the device. Moreover, trade-off between high photoresponsivity and response time is also responsible for slow speed ⁷⁻⁹. The present high photoresponsivity device is working on the mechanism of PTE which rely on thermal gradient which takes time to establish and relax. The thermalization and thermal diffusion of charge carriers at no external biasing may lead to response time of ~19 ms of the device. Despite these factors, the device exhibits fast response time than not only Photothermoelectric (PTE) devices but also than photovoltaic effect (PVE) and Photobolometric effect (PBE) based devices. (see Table S1).

Structure	Mechanism	Res./Rec. time	Ref.
SnTe films	PTE	78/48 ms	10
PbSe films	PTE	2.1/2.3s	11
PbTe nanosheets	PTE	2.71/4.4s	12
SnSe films	PBE	1.7/4.7 s	13
NiO/TiO ₂ /n-Si	PVE	0.1s	14
Au/NiO/n-Si/Au	PVE	266/200 ms	15
p-NiO/n-ZnO/n-Si	PVE	10.5/0.4 s	16
MoS ₂ /Graphene	PVE	20/30 ms	17
ZnO/NiO	PVE	7.5/4.8 s	18
Ti/n-Si/Au	PVE	12/16 ms	19

Reliability Test:

Reliability test helps to determine the potential of the device for its practical application.²⁰ The long life reliability of the device was determined through I-t of the device after six months. The device was placed under ambient conditions without packaging and protection measures during this time. It is found that the device performance remains stable after the duration of six months showing high stability, reproducibility and suitability of the device for its possible practical applications. Reliability test data of the device, before and after six months is given in Fig. S8a and S8b respectively.

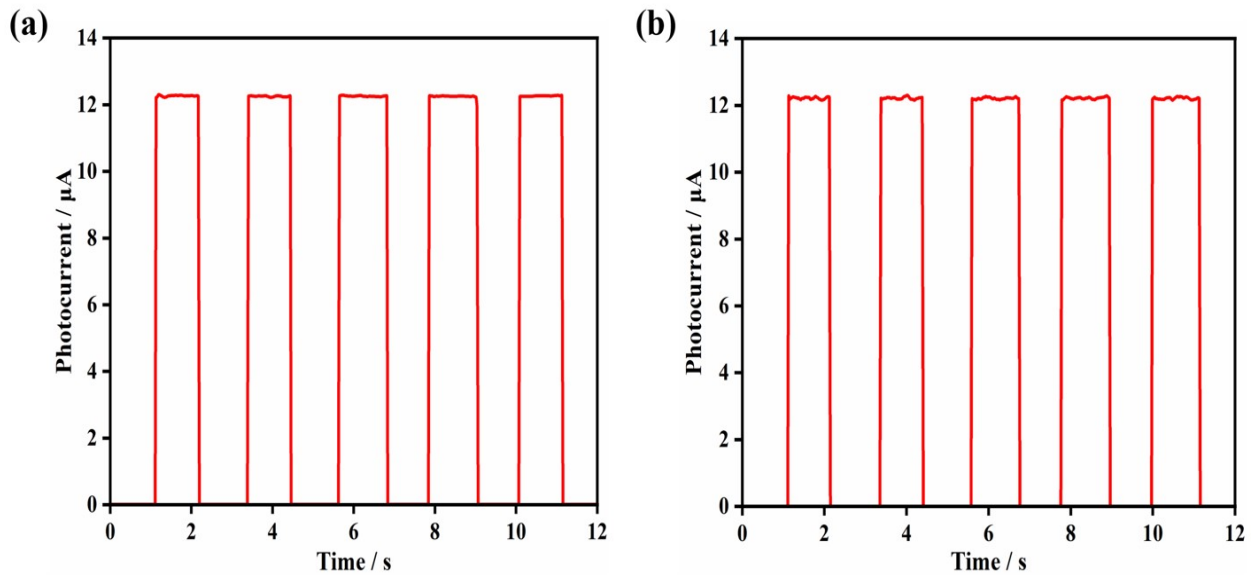


Fig. S8. Long life reliability test. (a) I-t curve six months before. (b) I-t curve of the device after six months under same conditions.

References:

1. H. Yuan, R. Lubbers, R. Besselink, M. Nijland and J. E. Ten Elshof, *ACS applied materials interfaces*, 2014, **6**, 8567-8574.
2. S. A. Hussain, B. Dey, D. Bhattacharjee and N. Mehta, *Heliyon*, 2018, **4**, e01038.
3. K. Akatsuka, M.-a. Haga, Y. Ebina, M. Osada, K. Fukuda and T. Sasaki, *ACS Nano*, 2009, **3**, 1097-1106.
4. T. Taniguchi, L. Nurdiwijayanto, R. Ma and T. Sasaki, *Applied Physics Reviews*, 2022, **9**.
5. D. Dudi, S. Ram Prakash, K. Bhardwaj, B. Aïssa and A. Mitra, *Optik*, 2024, **318**, 172093.
6. K. Wu, Y. Zhan, C. Zhang, S. Wu and X. Li, *Scientific reports*, 2015, **5**, 14304.
7. X. Ma, Y. Zhang, P. Tan, X. Feng, Y. Hao, G. Xu, X. Zhao, N. Gao, X. Hou, Q. Hu and S. Long, *n/a*, e70016.
8. K. S. Reddy B, S. Veeralingam, P. H. Borse and S. Badhulika, *Journal of Alloys and Compounds*, 2022, **919**, 165775.
9. N. R. Pradhan, J. Ludwig, Z. Lu, D. Rhodes, M. M. Bishop, K. Thirunavukkuarasu, S. A. McGill, D. Smirnov and L. Balicas, *ACS Applied Materials & Interfaces*, 2015, **7**, 12080-12088.
10. H. Liu, Y. Liu, S. Dong, H. Xu, Y. Wu, L. Hao, B. Cao, M. Li, Z. Wang, Z. Han and K. Yan, *ACS Applied Materials & Interfaces*, 2020, **12**, 49830-49839.
11. S. Peng, H. Li, C. Zhang, J. Han, X. Zhang, H. Zhou, X. Liu and J. Wang, 2022, **12**, 1391.
12. X. Zhao, Q. Yin, H. Huang, Q. Yu, B. Liu, J. Yang, Z. Dong, Z. Shen, B. Zhu, L. Liao and K. Zhang, *Nano Research*, 2021, **14**, 1955-1960.
13. H. Xu, L. Hao, H. Liu, S. Dong, Y. Wu, Y. Liu, B. Cao, Z. Wang, C. Ling, S. Li, Z. Xu, Q. Xue and K. Yan, *ACS Applied Materials & Interfaces*, 2020, **12**, 35250-35258.
14. X. Ma, L. Tang, Y. Zhang, W. Zuo, K. Seng Teng and G. Wu, *Infrared Physics & Technology*, 2024, **139**, 105305.
15. A. A. Ahmed, M. Devarajan and N. Afzal, *Sensors and Actuators A: Physical*, 2017, **262**, 78-86.
16. J.-D. Hwang and M.-C. Lin, *Sensors and Actuators A: Physical*, 2022, **349**, 114087.
17. Q. Liu, B. Cook, M. Gong, Y. Gong, D. Ewing, M. Casper, A. Stramel and J. Wu, *ACS Applied Materials & Interfaces*, 2017, **9**, 12728-12733.
18. Z. Zhang, Y. Ning and X. Fang, *Journal of Materials Chemistry C*, 2019, **7**, 223-229.
19. Y. J. Kim, M. R. Kumar, G. M. Kumar and M. Kim, *Applied Physics Letters*, 2023, **123**.
20. G. Xiang, J. Zhang, Z. Yue, X. Zhang, C. Song, B. Ding, L. Wang, Y. Wang, H. He, H. Wang and Y. Zhao, *Applied Surface Science*, 2023, **640**, 158397.